A Morphotropic Phase Boundary in $MA_{1-x}FA_xPbI_3$: Linking Structure, Dynamics, and Electronic Properties

Tobias Hainer, Erik Fransson, Sangita Dutta, Julia Wiktor, and Paul Erhart
*Department of Physics, Chalmers University of Technology, SE-41296, Gothenburg, Sweden**

Understanding the phase behavior of mixed-cation halide perovskites is critical for optimizing their structural stability and optoelectronic performance. Here, we map the phase diagram of $MA_{1-x}FA_xPbI_3$ using a machine-learned interatomic potential in molecular dynamics simulations. We identify a morphotropic phase boundary (MPB) at approximately 27 % FA content, delineating the transition between out-of-phase and in-phase octahedral tilt patterns. Phonon mode projections reveal that this transition coincides with a mode crossover composition, where the free energy landscapes of the M and R phonon modes become nearly degenerate. This results in nanoscale layered structures with alternating tilt patterns, suggesting minimal interface energy between competing phases. Our results provide a systematic and consistent description of this important system, complementing earlier partial and sometimes conflicting experimental assessments. Furthermore, density functional theory calculations show that band edge fluctuations peak near the MPB, indicating an enhancement of electron-phonon coupling and dynamic disorder effects. These findings establish a direct link between phonon dynamics, phase behavior, and electronic structure, providing a further composition-driven pathway for tailoring the optoelectronic properties of perovskite materials. By demonstrating that phonon overdamping serves as a hallmark of the MPB, our study offers new insights into the design principles for stable, high-performance perovskite solar cells.

In recent years, halide perovskites have garnered significant attention for their exceptional photovoltaic properties. These materials exhibit long carrier lifetimes [1–3] and high defect tolerance [4, 5], making them strong candidates for next-generation solar technologies. Their conversion efficiencies have exceeded 25 % [6], rivaling those of state-of-the-art solar cells. Moreover, their tunable bandgap and compositional flexibility allow precise control over optoelectronic properties [7, 8], enabling further enhancements in device performance.

Among the most promising halide perovskites are $MAPbI_3$ (methylammonium lead iodide) and $FAPbI_3$ (formamidinium lead iodide). $MAPbI_3$ has demonstrated high efficiency and ease of fabrication [9, 10], making it a benchmark material for perovskite solar cells. However, it suffers from limited thermal stability, undergoing phase transitions at elevated temperatures that degrade device performance [11]. In contrast, $FAPbI_3$ exhibits greater resistance to thermal decomposition [12, 13] and has a slightly lower bandgap, making it an attractive alternative. Nevertheless, its phase stability remains a challenge, as it readily transitions into non-perovskite phases at room temperature, limiting its photovoltaic potential [14, 15].

Mixing MA and FA cations to create $MA_{1-x}FA_xPbI_3$ has emerged as a strategy to combine the desirable properties of both materials. By tuning the MA-to-FA ratio, the structural stability, phase behavior, and electronic properties of the material can be optimized, achieving a balance between efficiency and stability [16]. This approach holds promise for developing perovskite materials that are both high-performing and durable under real-world conditions.

However, the introduction of mixed cations also adds complexity, and the phase diagram of the $MA_{1-x}FA_xPbI_3$ system remains incompletely understood. Experimentally probing these mixed phases has proven challenging, and no general consensus has been reached on their stability and transitions [17–21]. Yet, understanding these phase relationships is crucial for advancing the design of stable, high-efficiency perovskite solar cells.

Compositions rich in $MAPbI_3$ exhibit three distinct structural phases: a high-temperature cubic phase ($a^0a^0a^0$), a tetragonal phase with *out-of-phase* octahedral tilting ($a^0a^0c^-$), and a low-temperature orthorhombic phase ($a^-a^-c^+$). In contrast, $FAPbI_3$-rich compositions display two well-defined phases: a high-temperature cubic phase ($a^0a^0a^0$) and a tetragonal phase with *in-phase* tilting ($a^0a^0c^+$). Additionally, a low-temperature phase is observed, though its detailed structure remains uncertain [22]. Here, the Glazer notation [23], given in brackets, describes the tilt patterns of the PbI_6 octahedra.

A key observation is that the tetragonal phases of $MAPbI_3$ and $FAPbI_3$, which occur at room temperature, exhibit opposing tilt patterns ($a^0a^0c^-$ vs. $a^0a^0c^+$). Given the full miscibility of FA and MA, this suggests the presence of at least one morphotropic phase boundary (MPB). MPBs are well known in oxide perovskites and a key feature of many functional materials, particularly in ferroelectrics such as $PbZr_xTi_{1-x}O_3$, where they lead to enhanced piezoelectric and dielectric properties [24, 25]. While extensively studied in oxides, MPBs have received little attention in the context of halide perovskites, where their influence on phase behavior and optoelectronic properties remains largely unexplored. Identifying and characterizing this potential MPB could provide deeper

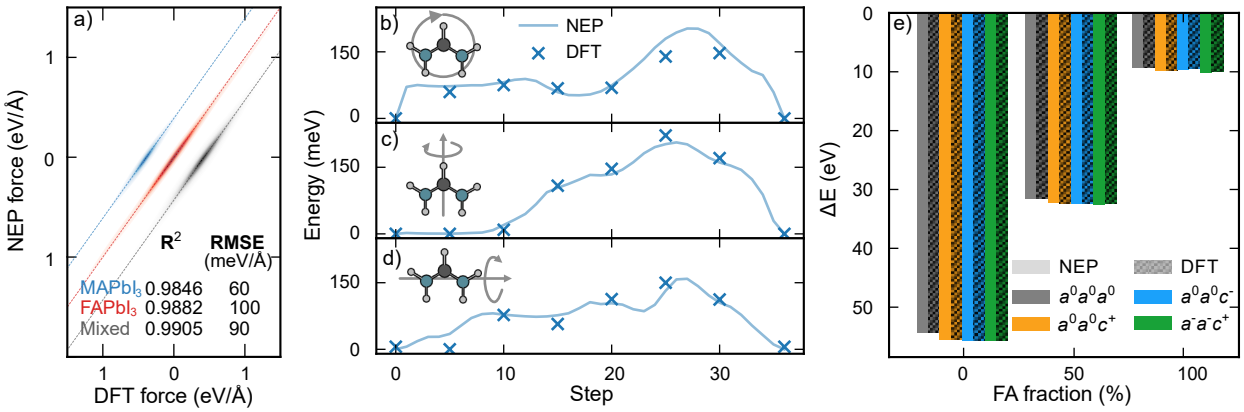

FIG. 1. **Machine-learned interatomic potential for $MA_{1-x}FA_xPbI_3$.** (a) Force parity plot, categorized by structure type. The different structure sets have been offset along the x-axis for clarity. (b–d) NEB calculations along three rotational paths, each corresponding to the rotation of a FA molecule around a different axis. (e) Energy differences between NEP model predictions and DFT calculations, grouped by FA fraction and color-coded by crystal structure.

insights into the structural dynamics of mixed-cation perovskites, clarify their impact on device performance, and introduce a new route for tuning optoelectronic properties through compositional engineering.

In this study, we investigate the phase diagram of $MA_{1-x}FA_xPbI_3$ using a machine-learned interatomic potential and molecular dynamics (MD) simulations to systematically map phase transitions and explore the underlying atomic-scale dynamics. Our results reveal the presence of a MPB at approximately 27 % FA, which separates the $a^0a^0c^-$ and $a^0a^0c^+$ phase regions. Notably, this boundary remains nearly invariant with temperature, indicating a robust compositional threshold between these structural phases.

We further analyze the role of soft (tilt) modes associated with these phases and find that they are heavily overdamped. Despite this, their signatures persist well into the high-temperature cubic phase ($a^0a^0a^0$), where remnants of these distortions remain detectable several hundred kelvins above the cubic-tetragonal phase transition. At low temperatures, our simulations indicate a single-phase region characterized by orthorhombic symmetry ($a^-a^-c^+$), further defining the stability of different structural regimes.

Finally, we demonstrate that the crossover in dynamics at the MPB significantly influences electron-phonon coupling, leading to a pronounced maximum in the fluctuation of the valence band maximum (VBM) level. This suggests that the particular soft phonon dynamics near the MPB may amplify dynamic disorder effects that are relevant to charge transport and optoelectronic performance. Our findings provide key insights into the complex phase behavior of mixed-cation perovskites and establish a framework for tuning their structural and electronic properties through composition engineering.

RESULTS AND DISCUSSION

A machine-learned interatomic potential for $MA_{1-x}FA_xPbI_3$

A computational study of the phase diagram of $MA_{1-x}FA_xPbI_3$ requires a model that is both accurate and efficient. Such a model must capture subtle energy differences between phases, account for the rotational dynamics of organic cations, and enable sampling of system dynamics across relevant length and time scales. To meet these requirements, we developed a machine-learned interatomic potential using the NEP approach (see the Methods section for details as well as Figs. S1, S2, and S3 of the SI).

Our NEP model achieves high accuracy, with root mean square errors of 3.9 meV atom^{-1}, 82 meV Å^{-1}, and 134 MPa for energies, forces (Fig. 1a), and stresses, respectively (also see Fig. S4 of the SI). The corresponding correlation coefficients (R^2) of 0.9997, 0.9896, and 0.9938 further demonstrate its precision. Additionally, the model accurately reproduces the rotational energy landscape of organic cations (Fig. 1b–d) and the energy differences between structural phases (Fig. 1e), making it well-suited for exploring phase behavior. Crucially, it is also computationally efficient, achieving a speed of up to 14×10^6 atom step s^{-1} on an Nvidia Ampere GPUs (including, e.g., the A100 and RTX3080 chips). With a time step of 0.5 fs, this corresponds to a simulation throughput of 6.3 ns d^{-1} for structures of 96 000 atoms, enabling large-scale molecular dynamics simulations.

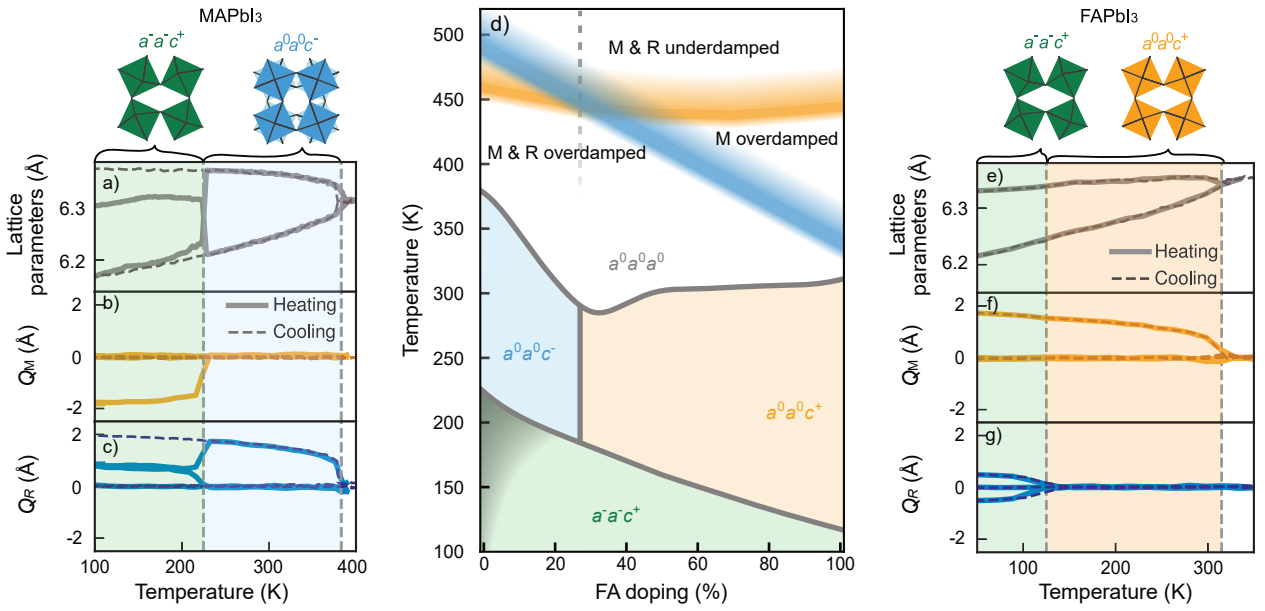

FIG. 2. **Phase diagram of $MA_{1-x}FA_xPbI_3$ from atomic-scale simulations.** (a–c) Lattice parameters and activation of M and R phonon modes during heating (solid lines) and cooling (dashed lines) of $MAPbI_3$. Dashed vertical lines indicate phase transitions. The tetragonal and orthorhombic phases observed during heating are illustrated by the PbI_6 octahedral tilt. (d) Predicted phase diagram based on phonon mode activation, labeled using Glazer notation. On the $MAPbI_3$ side the lower transition exhibits hysteresis due to its weak first-order character. The transition is therefore by a shaded area [26]. Regions of the cubic ($a^0a^0a^0$) phase are categorized as either overdamped or underdamped based on autocorrelation functions of the M and R modes. Note that the vertical line between the two tetragonal phases is the center of the MPB, and the dashed vertical lines is the mode crossover. (e–f) Lattice parameters and activation of M and R phonon modes during heating (solid lines) and cooling (dashed lines) of $FAPbI_3$, with tetragonal and orthorhombic phases illustrated as in $MAPbI_3$.

Phase diagram from mode projection

Initially, we explored the phases of the boundary compositions by performing heating and cooling MD simulations over a temperature range of 1 K to 400 K. From the resulting atomic trajectories, the displacements of iodine atoms were extracted and projected onto the R and M phonon modes of the cubic structure. This provided mode amplitudes, which were used to identify the tilt patterns and assign structural phases as a function of composition and temperature.

For $MAPbI_3$, phase transitions were identified based on abrupt changes in phonon mode activation, which correlated with variations in lattice parameters (Fig. 2a–c). At high temperatures, above approximately 385 K, the mode activation averages to zero consistent with a cubic $a^0a^0a^0$ structure. Between 385 K and 225 K, the R_z mode was activated during both heating and cooling, indicating a tetragonal $a^0a^0c^-$ structure. Below this temperature, heating and cooling trajectories diverged. During heating, the system adopted the orthorhombic $a^-a^-c^+$ structure, the generally accepted low-temperature phase of $MAPbI_3$ [27]. However, during cooling, the transition into the orthorhombic $a^-a^-c^+$ phase did not occur, consistent with a first-order phase transition with a large energy barrier [26]. While sufficient thermal energy allowed the system to overcome this barrier during heating, on the time scale of the MD simulations, it remained trapped in a metastable state upon cooling. Thus, the observed transition temperature serves as an upper bound.

In contrast, $FAPbI_3$ exhibited nearly identical behavior during heating and cooling(Fig. 2e–g), mainly due to our choice of starting structure when heating. This starting structure was chosen as the orthorhombic $a^-a^-c^+$ structure[22], which is the same structure recovered on cooling. Three distinct structural phases were identified(Fig. 2e–g): the cubic ($a^0a^0a^0$) phase, where no specific phonon mode activation was observed; the tetragonal ($a^0a^0c^+$) phase, characterized by M_z mode activation; and the orthorhombic ($a^-a^-c^+$) phase, where R_x, R_y, and M_z modes were all active.

By extending this procedure across the full composition range of $MA_{1-x}FA_xPbI_3$, a phase diagram was constructed (Fig. 2d). Across all compositions, cubic-to-tetragonal transitions occurred consistently during both heating and cooling, with structural changes following either the $a^0a^0a^0 \rightarrow a^0a^0c^-$ or $a^0a^0a^0 \rightarrow a^0a^0c^+$ pathways. Additionally, two tetragonal-to-orthorhombic transitions were identified: one between $a^0a^0c^-$ and

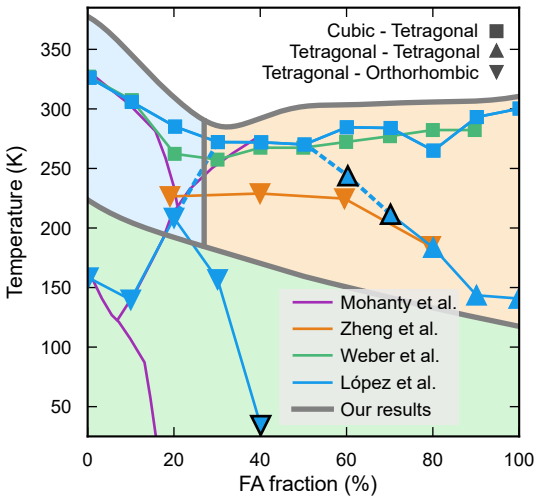

FIG. 3. **Comparison of simulated phase boundaries to experimental results.** Data points are represented by markers, with their shapes indicating the crystal structures involved in the phase transitions. Markers outlined in black correspond to measurements with a limited data basis. The results from Weber *et al.* [17] predict a cubic-tetragonal boundary that aligns well with the findings of Francisco-López *et al.* [18], who in addition to this identify several transitions at lower temperatures. Zheng *et al.* [19] propose a tetragonal-orthorhombic boundary throughout the intermediate temperature range (note that these data are for nanostructures). Mohanty *et al.* [20] report phase boundaries similar to those in other studies but classify the intermediate phase as "large-cell cubic".

$a^-a^-c^+$, and another between $a^0a^0c^+$ and $a^-a^-c^+$. The transition from $a^0a^0c^+$ to $a^-a^-c^+$ was observed in both heating and cooling simulations. However, the transition from $a^0a^0c^-$ to $a^-a^-c^+$ did not occur during cooling, indicating suppression, consistent with its first-order nature. Since this transition was only sampled during heating, the resulting transition temperature represents an upper bound. As a consequence, the precise temperature at which the orthorhombic phase becomes energetically favorable in this model remains uncertain. This uncertainty is indicated by the gray shaded region in the $MAPbI_3$-rich limit of the phase diagram (Fig. 2d). The lower bound of this region is guided by a previous free energy study of $MAPbI_3$, which identified the orthorhombic phase as the most stable structure below 90 K [26].

Comparison with experiment

To validate our predicted phase diagram, we compare the observed phase transitions with experimental studies compiled by Simenas *et al.* [21] (Fig. 3). This comparison allows us to assess the extent to which our simulations capture experimentally observed trends and resolve discrepancies in reported phase behavior.

The high-temperature cubic-tetragonal phase boundary aligns well with experimental observations, deviating primarily by a nearly constant offset across the entire composition range [17, 18, 28]. For $MAPbI_3$, the cubic, tetragonal, and orthorhombic phases identified here are consistent with previously reported structures. For $FAPbI_3$, the phase diagram confirms the known cubic and tetragonal phases while suggesting that the low-temperature phase adopts an orthorhombic $a^-a^-c^+$ symmetry reached on cooling.

Furthermore, our observations of the transition between two tetragonal symmetries, i.e., the presence of a MPB, are supported by experimental findings. Francisco-López *et al.* [18] observed a transition between two tetragonal symmetries at FA fractions 20 % to 30 % (see dashed blue line in Fig. 3). This agrees well with our placement of the MPB at the FA fraction 27 %. Mohanty *et al.* [20] also identified a transition in this region, but instead of transitioning between two tetragonal structures they assigned a transition between a tetragonal and a "large-cell cubic" structure.

The intermediate composition range of $MA_{1-x}FA_xPbI_3$ below the cubic phase region has been challenging to probe experimentally. In this region, our simulations indicate the presence of tetragonal and orthorhombic structures. Based on temperature-dependent photoluminescence measurements on nanostructures, Zheng *et al.* [19] reported tetragonal-to-orthorhombic transitions at FA concentrations of 20 % to 80 %, consistent with the trends observed in this study. However, conflicting experimental findings exist for this region. The results from Francisco-López *et al.* [18] using photoluminescence and Raman scattering suggest that there are no orthorhombic structures above 40 % FA fraction, instead assigning this region a possibly tetragonal symmetry and adding that there is disorder present. Note, however, that these assignments are not based on crystallographic analysis. Furthermore, an additional study using X-ray diffraction from Mohanty *et al.* [20] indicates a "large-cubic symmetry" for large parts of this intermediate region. These discrepancies highlight the challenges in experimentally resolving the phase behavior of mixed-cation perovskites, further emphasizing the role of atomistic simulations in providing complementary insights.

We note, however, that the results from Francisco-López *et al.* could be interpreted as supporting our findings. Their Raman scattering results indicate clear phase transitions between tetragonal and orthorhombic phases for FA fractions 0 % to 30 % at temperatures between approximately 130 K to 210 K (indicated by the blue inverted triangles in Fig. 3). However, the measurement at FA fraction 40 %, which suggests a similar transition near 40 K, is less conclusive (indicated with a black outline in

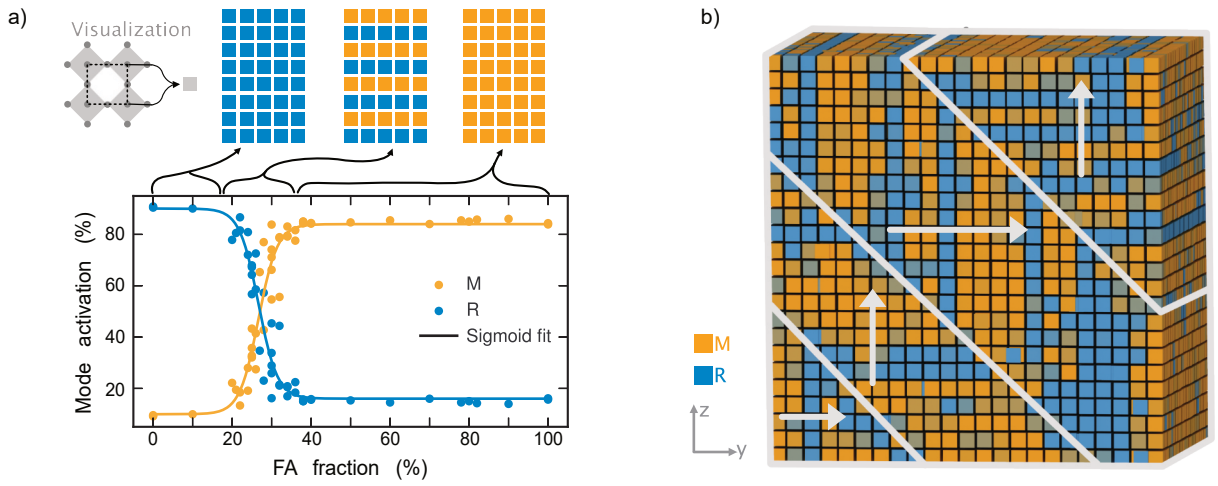

FIG. 4. **Dynamics at the morphotropic phase boundary.** (a) Mode activation as a function of FA doping at 250 K, illustrating the smooth transition between dominant phonon modes at the MPB. Structural schematics depict different regions, where each square represents a unit cell and is color-coded based on the frozen-in phonon mode: blue for R mode and orange for M mode. For low FA doping, the R mode is dominant throughout the system, while for high FA doping, the M mode prevails. At the MPB, both modes are active and arrange into layered structures. (b) Mode activation in $MA_{0.73}FA_{0.27}PbI_3$ from a large-scale simulation of 1.3 million atoms cooled to 260 K. Twinning behavior is observed, forming two distinct regions: one dominated by modes along the z-direction and the other along the y-direction, indicated by arrows. Within each region, alternating layers of M and R modes emerge, consistent with the layered structures identified in smaller simulations near the MPB.

the Fig. 3). A similar ambiguity exists for transitions on the FA-rich side of the phase diagram. Here, photoluminescence peak energy shifts have been interpreted as a transition from tetragonal symmetry to a phase described as disordered and possibly tetragonal between roughly 130 K to 200 K for FA fractions of 80 % to 100 % (blue triangles in Fig. 3). Transitions are also assigned for 60 % and 70 % FA. These are however not as clear, which is explained by the transition being continuous (marked with black outlines in Fig. 3). Excluding this less conclusive Raman and photoluminescence data, we find a tetragonal-orthorhombic phase boundary for FA fractions of 0 % to 30 % (130 K to 210 K) and a transition to a phase indexed as tetragonal for 80 % to 100 % (130 K to 200 K). However, the assignment of this tetragonal symmetry on the FA-rich side was tentative [17, 29, 30], and their neutron diffraction patterns did not allow for a complete classification of the unit cell symmetry. Given this, along with recent evidence suggesting that the low-temperature phase of $FAPbI_3$ is orthorhombic [22], it is reasonable to reconsider the classification of this FA-rich region as orthorhombic. This is also in line with the analysis of Zheng *et al.*, which connects the two sides of the phase diagram through a tetragonal-orthorhombic phase boundary. So, if one takes into account the uncertainty associated with data points obtained by Francisco-López *et al.*, it results in a phase diagram consistent with our simulations.

Character of the morphotropic phase boundary

The phase diagram suggests a transition driven purely by compositional change —a MPB— between the $a^0a^0c^-$ and $a^0a^0c^+$ structures, corresponding to the vertical boundary between these phases (Fig. 2). Such a transition is inevitable in the phase diagram of this alloy, as the distinct phases of the boundary compositions cannot be combined without forming at least one MPB.

To investigate the MPB, we calculated and normalized the activation of the phonon modes along the primary tilt axis at 250 K (Fig. 4a). For compositions with FA doping significantly above or below the MPB, the system exhibited a strong preference for either the M_z or R_z modes, consistent with the expected $a^0a^0c^+$ and $a^0a^0c^-$ crystal structures. However, in the intermediate region, a smooth transition between the two modes was observed. The midpoint of this transition, corresponding to an FA doping of 27 %, defines the center of the MPB.

The phonon mode projections provided detailed insights into the structural characteristics at the MPB. Analysis of the transition pathway between M_z and R_z-dominated regions revealed the formation of alternating layers of either tilt pattern (Fig. 4a). These layers, aligned along the primary tilt axis, were nearly exclusively populated by either M_z or R_z modes, explaining the observed smooth transition. At the center of the MPB, an equal number of layers populated by M_z and R_z was present, marking the compositional crossover point.

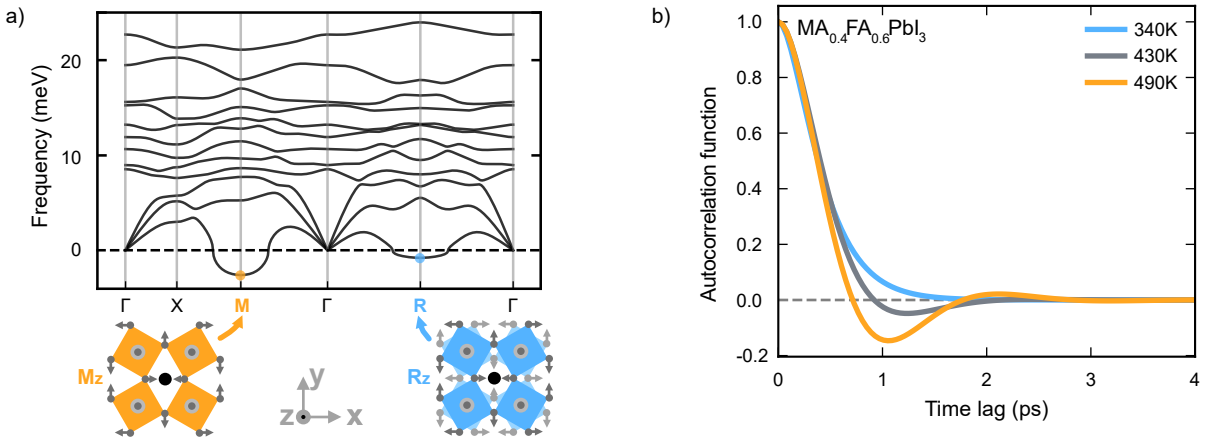

FIG. 5. **Phonon dispersion and overdamping.** (a) Phonon dispersion of $MAPbI_3$ in the cubic phase. The displacement patterns corresponding to the imaginary modes at the M and R points (indicated by negative frequencies) are illustrated, with arrows representing the displacement of iodine atoms. In the M_z mode, octahedral layers tilt uniformly in the same direction, whereas in the R_z mode, adjacent layers tilt alternately in opposite directions (dark and light gray arrows). (b) The ACF of the R mode for $MA_{0.4}FA_{0.6}PbI_3$ at 340 K, 430 K and 490 K, illustrating the transition from under to overdamped dynamics with decreasing temperature.

As discussed in the next section, the emergence of these layers at the MPB is a consequence of the nearly degenerate free energy landscape for M and R modes when transitioning from the cubic to the tetragonal phase. Below the transition temperature, these modes freeze in, resulting in a layered distribution proportional to their likelihood at the transition.

Since the well-defined layered structures observed at the MPB could be influenced by the limited size of smaller simulations, we conducted large-scale simulations using a system of 1.3 million atoms. These systems were initialized in the cubic phase and cooled to temperatures where the MPB emerges. For $MA_{0.73}FA_{0.27}PbI_3$, two distinct regions formed, stacked along the ⟨011⟩ direction, each exhibiting layered M and R mode activation (Fig. 4b). These regions were distinguished by a 90° rotation, with the modes within each domain aligned along alternating directions.

The domains exhibited a characteristic width of approximately 20 nm, although this was likely influenced by the finite size of the simulation box, as the maximum system length along the ⟨011⟩ direction was roughly 40 nm.

The layered structures and domain formations at the MPB point toward a structurally soft regime where the energy landscape between competing phases is shallow. Unlike classical ferroelectric perovskites, where ferroelectric, ferroelastic, and even ferromagnetic properties are maximized at the MPB [31], the present system does not exhibit intrinsic ferroelectricity. Instead, the presence of MPB-associated soft lattice dynamics may play a key role in optoelectronic properties as discussed further below, particularly through their influence on dynamic disorder and electron-phonon coupling.

The formation of 90° domain walls along the ⟨011⟩ direction, a feature previously observed in perovskites with ferroelastic and ferroelectric character [32, 33], may suggest an intrinsic structural response to local stresses or instabilities. However, rather than long-range polarization, these domains likely reflect the ability of the system to accommodate structural frustration through dynamically fluctuating tilt patterns.

This complex domain morphology and the presence of internally modulated structural distortions further explain why experimental determination of the crystal structure of $MA_{1-x}FA_xPbI_3$ has been particularly challenging. Regions with different orientations, coupled with internal layers of frozen or fluctuating tilt modes, introduce a level of disorder that complicates conventional diffraction-based classification.

Phonon mode dynamics

The dynamics of phonons play a fundamental role in determining the optoelectronic properties of halide perovskites. In particular, the extent of phonon damping —whether a mode is underdamped or overdamped— directly influences electron-phonon coupling and charge carrier behavior [34]. Since the electron-phonon coupling matrix element scales inversely with the square root of the phonon frequency, soft phonon modes can significantly enhance electron-phonon interactions. Thus, regions of the phase diagram where phonons soften, such as near phase boundaries and the MPB, are expected to exhibit strong dynamic disorder effects that influence the electronic structure.

To further investigate this, the boundaries between underdamped and overdamped phonon behavior were analyzed across the composition range. This allows for the identification of regions where phonon damping transitions occur, providing insight into where dynamic fluctuations are most likely to affect optoelectronic properties.

A phonon mode is underdamped when its oscillatory behavior persists over multiple cycles before decaying, meaning the system retains a well-defined vibrational coherence. In contrast, a phonon mode is overdamped when its oscillations are suppressed, and the mode decays before completing a full cycle. This transition occurs when the damping rate exceeds the vibrational frequency, effectively transforming the phonon into a non-propagating relaxation mode.

In perovskites, phonon modes can become overdamped near structural phase transitions, where the potential energy surface flattens and vibrational modes soften. This has been observed in related materials such as $CsPbBr_3$, where overdamped phonons persist well above phase transition temperatures, leading to enhanced dynamic disorder and influencing charge transport properties [35, 36]. Given that soft phonon modes enhance electron-phonon coupling, mapping overdamped and underdamped regions provides direct insight into where electronic properties —such as band structure renormalization, charge transport, and recombination rates— are most strongly affected by lattice dynamics.

To determine whether a phonon mode was underdamped or overdamped, its ACF was calculated, and the decay characteristics were extracted. A damped harmonic oscillator fit was applied to obtain the decay time and oscillation frequency, allowing classification of each mode. The ACF fits for the R mode of $MA_{0.4}FA_{0.6}PbI_3$ can be seen for three different temperatures in Fig. 5. This illustrates how the oscillation vanishes when decreasing temperature, indicating a transition of the ACF from being an underdamped to overdamped oscillator. Extending this analysis across the entire composition range allowed for the identification of the boundaries between underdamped and overdamped regions in the phase diagram (Fig. 2d).

Three distinct dynamic regions emerged. At high temperatures, both M and R modes were underdamped, retaining vibrational coherence. At lower temperatures, both modes became fully overdamped, losing coherence due to strong phonon damping. An intermediate region was identified where only the M mode was overdamped, revealing an asymmetry in how phonon dynamics evolve with composition and temperature. Notably, there exists a specific composition at which the transition from underdamped to overdamped dynamics occurs at the same temperature. At this composition, the free energy landscapes of the M and R modes become nearly degenerate, allowing the system to dynamically fluctuate between in-phase and out-of-phase octahedral tilting. This composition of mode crossover coincides with the MPB, suggesting that the onset of phonon overdamping may serve as a hallmark of the MPB. Indeed, as shown above, the structure at the MPB exhibits a mixture of layers with M and R tilting at very short periodicity (Fig. 4), indicating that the interface energy between these tilting patterns becomes vanishingly small.

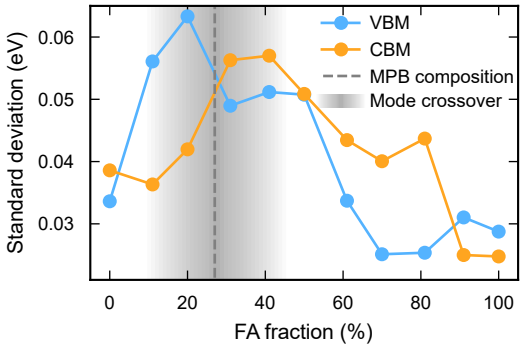

FIG. 6. **Effective electron-phonon coupling strength.** Standard deviations of the VBM and CBM levels as a function of FA composition at 330 K. The variation of the band edges becomes maximal in the range from 20 to 40 % FA and thus in the vicinity of the MPB.

The identification of overdamped and underdamped phonon regions has direct consequences for electronic transport and optical properties. Since the electron-phonon coupling matrix element scales inversely with the square root of the phonon frequency, soft phonons can enhance electron-phonon interactions. One can therefore expect regions where phonons become overdamped to often coincide with enhanced charge carrier interactions with lattice vibrations, leading to strong phonon anharmonicity and dynamic disorder. These effects can significantly impact band structure, carrier scattering, and defect tolerance. As halide perovskites are frequently used in solar cells and optoelectronic devices operating well above room temperature, understanding phonon dynamics at elevated temperatures is crucial for predicting device performance and stability. By mapping phonon damping transitions, this analysis provides a framework for anticipating temperature and composition-dependent changes in optoelectronic behavior, guiding future experiments and theoretical studies.

Electronic structure

To investigate the impact of octahedral and cation dynamics on the electronic structure, we performed DFT calculations on representative snapshots from NEP-MD simulations at 330 K. To quantify the effective strength of electron-phonon coupling under these conditions — i.e., in metastable (dynamically stabilized) structures at

finite temperature— we computed the standard deviation of the VBM and CBM energies across the sampled structures as a function of FA content (Fig. 6).

In general, band edge fluctuations are more pronounced in mixed compositions than in pure phases, with the largest variations in the VBM and CBM occurring around 20 % and 40 % FA, respectively. These enhanced fluctuations suggest an increased potential for carrier localization, as variations in the electronic structure can create local energy minima that trap charges. Notably, this non-monotonic behavior of electron-phonon coupling emerges in the cubic phase near the mode crossover composition and, consequently, the MPB (Fig. 2d). Since these two phenomena are intrinsically linked, as discussed above, this suggests that systems exhibiting MPBs are also likely to show enhanced electron-phonon coupling— providing a structural mechanism for tuning optoelectronic properties.

CONCLUSIONS

In this study, we systematically mapped the phase diagram of $MA_{1-x}FA_xPbI_3$ using machine-learned interatomic potentials and MD simulations. Our results reveal the presence of a MPB at approximately 27 % FA content, marking the transition between out-of-phase and in-phase octahedral tilt patterns. This MPB remains nearly invariant with temperature, highlighting its compositional stability and structural significance.

Phonon mode analysis demonstrated that M and R phonon modes exhibit distinct overdamping behavior, with a mode crossover composition aligning with the MPB. This transition is accompanied by the formation of nanoscale layered structures with alternating tilt patterns, indicative of vanishingly small interface energies between competing structural motifs. These findings provide a structural explanation for the phase coexistence observed in this region.

Furthermore, our results offer a systematic and consistent description of the phase behavior of $MA_{1-x}FA_xPbI_3$, helping to reconcile previous partial and sometimes conflicting experimental assessments of this system. By providing a detailed, atomistic-level understanding of structural transitions and phonon dynamics, our work complements experimental efforts that have faced challenges in fully resolving the phase relationships of mixed-cation perovskites.

We also explored the implications for electron-phonon interactions, finding that band edge fluctuations peak near the MPB, suggesting an enhancement of dynamic disorder and charge carrier localization. These results establish a direct link between phonon dynamics, phase behavior, and electronic structure, introducing MPBs as a structural tuning mechanism for optoelectronic properties.

By demonstrating that phonon overdamping serves as a hallmark of the MPB, our study provides new insights into composition-driven strategies for tuning the stability and performance of perovskite materials. This framework contributes to the rational design of high-performance perovskite solar cells, where fine-tuning structural dynamics can play a key role in optimizing optoelectronic properties.

METHODS

Machine-learned interatomic potential

We constructed a machine-learned interatomic potential based on the fourth-generation NEP framework [37, 38] using the iterative procedure described in Ref. 39 utilizing the GPUMD [37] and CALORINE packages [40]. The training set was initially composed of both systematically and randomly strained and scaled structures, based on ideal structures (see the Zenodo record for a database of all structures used). An initial model was trained on all available data.

The dataset was then augmented with structures from several iterations of active learning. To this end, we additionally trained an ensemble of five models by randomly splitting the available data into training and validation sets. The ensemble was used to estimate the model error. MD simulations were then carried out at a range of temperatures and pressures considering compositions over the entire concentration range. The ensemble was used to select structures with a high uncertainty, quantified by the standard deviations of energies and forces over the ensemble. Subsequently we computed energies, forces, and stresses via DFT for these configurations and included them when training the next-generation NEP model. In total the training set comprised 986 structures, corresponding to a total of 179 018 atoms. Structures were generated and manipulated using the ASE [41] and HIPHIVE packages [42].

For the NEP model radial and angular cutoffs were set to 8 Å and 4 Å, respectively, and angular descriptors included both three and four-body components. The neural network architecture consisted of 30 descriptor nodes in the input layer (5 radial, 25 angular) and one hidden layer with 30 fully connected neurons. The final model was trained using the separable neuroevolution strategy [43] for 10^6 generations, after which the loss, based on the root-mean-squared errors, was deemed converged (Fig. S1; also see Figs. S2 and S3 of the SI). The model performance is illustrated in Fig. 1 and Fig. S4.

Density functional theory calculations

The NEP model was fitted using forces, energies, and virials obtained from DFT calculations, employing the SCAN+rVV10 exchange-correlation functional [44] as implemented in the Vienna ab-initio simulation package [45, 46] using projector-augmented wave [47, 48] setups with a plane wave energy cutoff of 520 eV. The Brillouin zone was sampled with automatically generated Γ-centered $\boldsymbol{k}$-point grids with a maximum spacing of 0.15 Å^{-1}.

Molecular dynamics simulations

Structures were constructed from a 96-atom cell, corresponding to a $2 \times 2 \times 2$ primitive cubic unit cell, comprising 24 iodine atoms, 8 lead atoms, and 12 MA or FA molecules. The initial unit cell symmetry, defined by iodine displacements, was set to cubic ($a^0a^0a^0$) for cooling simulations and orthorhombic ($a^-a^-c^+$) for heating simulations. To obtain the desired system size, the structure was replicated along its axes. Random molecular substitutions were performed to achieve the target $MAPbI_3$:$FAPbI_3$ ratio, ensuring no spatial correlation in the MA/FA distribution.

MD simulations were carried out using the GPUMD package with a time step of 0.5 fs. The simulations employed the NPT ensemble via a Langevin thermostat and a stochastic cell rescaling barostat [49]. To construct the phase diagram, heating and cooling simulations were conducted between 1 K and 400 K at rates ranging from 7 K ns^{-1} to 15 K ns^{-1}.

To assess finite-size effects, we monitored the lattice parameters of pure $MAPbI_3$ and $FAPbI_3$ as a function of supercell size. These convergence tests showed that supercells with at least 12 000 atoms were sufficient to obtain reliable results. for phase diagram construction we therefore used supercells ranging from 12 000 to 96 000 atoms.

To examine the impact of octahedral and cation dynamics on the electronic structure, we performed MD simulations using the NEP model in a 768-atom supercell at 330 K with a fixed cell shape and volume. This temperature was chosen because, the tetragoanl-cubic phase boundary occurs at slightly higher temperatures than observed experimentally. We investigated MA/FA mixing ratios with FA fractions of 0 %, 11 %, 20 %, 31 %, 41 %, 50 %, 61 %, 70 %, 81 %, and 100 %. From each MD trajectory, we selected 20 snapshots and computed the electronic structure using DFT, sampling k-space only at the Γ point while maintaining consistency with training runs. We then extracted the positions of the VBM and CBM to quantify their fluctuation magnitudes.

Phonon mode projection

To classify the local crystal structure along a MD trajectory, we employed local phonon mode projection to quantify atomic displacements relative to the ideal cubic perovskite structure. The analysis focused on the M and R phonon modes, which correspond to the tilting of PbI_6 octahedra in the 96-atom unit cell. These modes are three-fold degenerate, denoted as $M_{x/y/z}$ and $R_{x/y/z}$, depending on the tilt axis (see Fig. 5 for an illustration of M_z and R_z). To quantify mode activation, the displacement of each iodine atom from the ideal cubic structure, $\boldsymbol{u}$, was projected onto the M and R mode eigenvectors, $\boldsymbol{e}_{\text{M/R}}$, yielding $Q_{\text{M/R}} = \boldsymbol{u} \cdot \boldsymbol{e}_{\text{M/R}}$. The resulting phonon mode activation was normalized by dividing $Q_{\text{M/R}}$ by the number of iodine atoms per unit cell. This normalization ensures that the activation represents the average iodine displacement along the phonon mode.

DATA AVAILABILITY

The NEP model as well as the database of DFT calculations used to train this model are available on zenodo at `https://doi.org/10.5281/zenodo.14992798`.

ACKNOWLEDGMENTS

We gratefully acknowledge funding from the Swedish Research Council (Nos. 2019-03993, 2020-04935 and 2021-05072), the Knut and Alice Wallenberg Foundation (Nos. 2023.0032 and 2024.0042), the Swedish Strategic Research Foundation (FFL21-0129), and the European Research Council (ERC Starting Grant No. 101162195) as well as computational resources provided by the National Academic Infrastructure for Supercomputing in Sweden at NSC, PDC, and C3SE partially funded by the Swedish Research Council through grant agreement No. 2022-06725, as well as the Berzelius resource provided by the Knut and Alice Wallenberg Foundation at NSC.

COMPETING INTERESTS

All authors declare no financial or non-financial competing interests.

* erhart@chalmers.se

[1] C. S. Ponseca, T. J. Savenije, M. Abdellah, K. Zheng, A. Yartsev, T. Pascher, T. Harlang, P. Chabera, T. Pullerits, A. Stepanov, J.-P. Wolf, and V. Sundström, Organometal Halide Perovskite Solar Cell Materials

Rationalized: Ultrafast Charge Generation, High and Microsecond-Long Balanced Mobilities, and Slow Recombination, Journal of the American Chemical Society **136**, 5189 (2014).

[2] E. Edri, S. Kirmayer, S. Mukhopadhyay, K. Gartsman, G. Hodes, and D. Cahen, Elucidating the charge carrier separation and working mechanism of $CH_3NH_3PbI_{3-x}Cl_x$ perovskite solar cells, Nature Communications **5**, 3461 (2014).

[3] Y. Bi, E. M. Hutter, Y. Fang, Q. Dong, J. Huang, and T. J. Savenije, Charge Carrier Lifetimes Exceeding 15 µs in Methylammonium Lead Iodide Single Crystals, The Journal of Physical Chemistry Letters **7**, 923 (2016).

[4] G. Kim and A. Petrozza, Defect Tolerance and Intolerance in Metal-Halide Perovskites, Advanced Energy Materials **10**, 2001959 (2020).

[5] J. Kang and L.-W. Wang, High Defect Tolerance in Lead Halide Perovskite $CsPbBr_3$, The Journal of Physical Chemistry Letters **8**, 489 (2017).

[6] Best Research-Cell Efficiency Chart, `https://www.nrel.gov/pv/cell-efficiency.html`; accessed: 2024-11-14.

[7] S. A. Kulkarni, T. Baikie, P. P. Boix, N. Yantara, N. Mathews, and S. Mhaisalkar, Band-gap tuning of lead halide perovskites using a sequential deposition process, Journal of Materials Chemistry A **2**, 9221 (2014).

[8] D. B. Straus and R. J. Cava, Tuning the Band Gap in the Halide Perovskite $CsPbBr_3$ through Sr Substitution, ACS Applied Materials & Interfaces **14**, 34884 (2022).

[9] Q. Chen, H. Zhou, Z. Hong, S. Luo, H.-S. Duan, H.-H. Wang, Y. Liu, G. Li, and Y. Yang, Planar Heterojunction Perovskite Solar Cells via Vapor-Assisted Solution Process, Journal of the American Chemical Society **136**, 622 (2014).

[10] N. K. Noel, S. N. Habisreutinger, B. Wenger, M. T. Klug, M. T. Hörantner, M. B. Johnston, R. J. Nicholas, D. T. Moore, and H. J. Snaith, A low viscosity, low boiling point, clean solvent system for the rapid crystallisation of highly specular perovskite films, Energy & Environmental Science **10**, 145 (2017).

[11] T. T. Ava, A. Al Mamun, S. Marsillac, and G. Namkoong, A Review: Thermal Stability of Methylammonium Lead Halide Based Perovskite Solar Cells, Applied Sciences **9**, 188 (2019).

[12] Z. Qiu, N. Li, Z. Huang, Q. Chen, and H. Zhou, Recent Advances in Improving Phase Stability of Perovskite Solar Cells, Small Methods **4**, 1900877 (2020).

[13] Y. Li, A. Bahnick, P. J. Lohr, S. Raglow, and A. D. Printz, Enhanced α-phase stability of formamidinium lead iodide with addition of 5-ammonium valeric acid chloride, Energy Advances **4**, 262 (2024).

[14] T. Niu, L. Chao, X. Dong, L. Fu, and Y. Chen, Phase-Pure α-$FAPbI_3$ for Perovskite Solar Cells, The Journal of Physical Chemistry Letters **13**, 1845 (2022).

[15] Z. Zheng, S. Wang, Y. Hu, Y. Rong, A. Mei, and H. Han, Development of formamidinium lead iodide-based perovskite solar cells: efficiency and stability, Chemical Science **13**, 2167 (2022).

[16] B. Charles, J. Dillon, O. J. Weber, M. S. Islam, and M. T. Weller, Understanding the stability of mixed A-cation lead iodide perovskites, Journal of Materials Chemistry A **5**, 22495 (2017).

[17] O. J. Weber, B. Charles, and M. T. Weller, Phase behaviour and composition in the formamidinium–methylammonium hybrid lead iodide perovskite solid solution, Journal of Materials Chemistry A **4**, 15375 (2016).

[18] A. Francisco-López, B. Charles, M. I. Alonso, M. Garriga, M. Campoy-Quiles, M. T. Weller, and A. R. Goñi, Phase Diagram of Methylammonium/Formamidinium Lead Iodide Perovskite Solid Solutions from Temperature-Dependent Photoluminescence and Raman Spectroscopies, The Journal of Physical Chemistry C **124**, 3448 (2020).

[19] H. Zheng, J. Dai, J. Duan, F. Chen, G. Zhu, F. Wang, and C. Xu, Temperature-dependent photoluminescence properties of mixed-cation methylammonium–formamidium lead iodide $[HC(NH_2)_2]_x[CH_3NH_3]_{1-x}PbI_3$ perovskite nanostructures, Journal of Materials Chemistry C **5**, 12057 (2017).

[20] A. Mohanty, D. Swain, S. Govinda, T. N. G. Row, and D. D. Sarma, Phase diagram and dielectric properties of $MA_{1-x}FA_xPbI_3$, ACS Energy Letters **4**, 2045 (2019).

[21] M. Simenas, A. Gagor, J. Banys, and M. Maczka, Phase Transitions and Dynamics in Mixed Three- and Low-Dimensional Lead Halide Perovskites, Chemical Reviews **124**, 2281 (2024).

[22] S. Dutta, E. Fransson, T. Hainer, B. M. Gallant, D. Kubicki, P. Erhart, and J. Wiktor, Large-scale machine learning reveals the structure of the low-temperature phase of $FAPbI_3$ (2025), to be submitted.

[23] A. M. Glazer, The classification of tilted octahedra in perovskites, Acta Crystallographica Section B: Structural Crystallography and Crystal Chemistry **28**, 3384 (1972).

[24] A. P. S. S. K. Mishra and D. Pandey, Thermodynamic nature of phase transitions in $Pb(Zr_xTi_{1-x})O_3$ ceramics near the morphotropic phase boundary. i. structural studies, Philosophical Magazine B **76**, 213 (1997).

[25] B. Noheda, D. E. Cox, G. Shirane, J. A. Gonzalo, L. E. Cross, and S.-E. Park, A monoclinic ferroelectric phase in the $Pb(Zr_{1-x}Ti_x)O_3$ solid solution, Applied Physics Letters **74**, 2059 (1999).

[26] E. Fransson, J. M. Rahm, J. Wiktor, and P. Erhart, Revealing the Free Energy Landscape of Halide Perovskites: Metastability and Transition Characters in $CsPbBr_3$ and $MAPbI_3$, Chemistry of Materials **35**, 8229 (2023).

[27] P. S. Whitfield, N. Herron, W. E. Guise, K. Page, Y. Q. Cheng, I. Milas, and M. K. Crawford, Structures, Phase Transitions and Tricritical Behavior of the Hybrid Perovskite Methyl Ammonium Lead Iodide, Scientific Reports **6**, 35685 (2016).

[28] D. J. Kubicki, D. Prochowicz, A. Hofstetter, P. Péchy, S. M. Zakeeruddin, M. Grätzel, and L. Emsley, Cation Dynamics in Mixed-Cation $(MA)_x(FA)_{1-x}PbI_3$ Hybrid Perovskites from Solid-State NMR, Journal of the American Chemical Society **139**, 10055 (2017).

[29] T. Chen, B. J. Foley, C. Park, C. M. Brown, L. W. Harriger, J. Lee, J. Ruff, M. Yoon, J. J. Choi, and S.-H. Lee, Entropy-driven structural transition and kinetic trapping in formamidinium lead iodide perovskite, Science Advances **2**, e1601650 (2016).

[30] O. J. Weber, D. Ghosh, S. Gaines, P. F. Henry, A. B. Walker, M. S. Islam, and M. T. Weller, Phase Behavior and Polymorphism of Formamidinium Lead Iodide, Chemistry of Materials **30**, 3768 (2018).

[31] R. E. Newnham, *Properties of Materials: Anisotropy, Symmetry, Structure* (Oxford University Press, Oxford, UK, 2005).

[32] W. J. Merz, Domain Formation and Domain Wall Motions in Ferroelectric $BaTiO_3$ Single Crystals, Physical

Review **95**, 690 (1954).
[33] E. A. Little, Dynamic Behavior of Domain Walls in Barium Titanate, Physical Review **98**, 978 (1955).
[34] X. Zhu and D. A. Egger, Effect of overdamped phonons on the fundamental band gap of perovskites, Phys. Rev. Lett. **134**, 016403 (2025).
[35] T. Lanigan-Atkins, X. He, M. J. Krogstad, D. M. Pajerowski, D. L. Abernathy, G. N. M. N. Xu, Z. Xu, D.-Y. Chung, M. G. Kanatzidis, S. Rosenkranz, R. Osborn, and O. Delaire, Two-dimensional overdamped fluctuations of the soft perovskite lattice in CsPbBr3, Nature Materials **20**, 977 (2021).
[36] E. Fransson, P. Rosander, F. Eriksson, J. M. Rahm, T. Tadano, and P. Erhart, Limits of the phonon quasiparticle picture at the cubic-to-tetragonal phase transition in halide perovskites, Communications Physics **6**, 173 (2023).
[37] Z. Fan, Y. Wang, P. Ying, K. Song, J. Wang, Y. Wang, Z. Zeng, K. Xu, E. Lindgren, J. M. Rahm, A. J. Gabourie, J. Liu, H. Dong, J. Wu, Y. Chen, Z. Zhong, J. Sun, P. Erhart, Y. Su, and T. Ala-Nissila, GPUMD: A package for constructing accurate machine-learned potentials and performing highly efficient atomistic simulations, The Journal of Chemical Physics **157**, 114801 (2022).
[38] K. Song, R. Zhao, J. Liu, Y. Wang, E. Lindgren, Y. Wang, S. Chen, K. Xu, T. Liang, P. Ying, N. Xu, Z. Zhao, J. Shi, J. Wang, S. Lyu, Z. Zeng, S. Liang, H. Dong, L. Sun, Y. Chen, Z. Zhang, W. Guo, P. Qian, J. Sun, P. Erhart, T. Ala-Nissila, Y. Su, and Z. Fan, General-purpose machine-learned potential for 16 elemental metals and their alloys, Nature Communications **15**, 10208 (2024).
[39] E. Fransson, J. Wiktor, and P. Erhart, Phase Transitions in Inorganic Halide Perovskites from Machine-Learned Potentials, The Journal of Physical Chemistry C **127**, 13773 (2023).
[40] E. Lindgren, M. Rahm, E. Fransson, F. Eriksson, N. Österbacka, Z. Fan, and P. Erhart, calorine: A Python package for constructing and sampling neuroevolution potential models, Journal of Open Source Software **9**, 6264 (2024).
[41] A. Hjorth Larsen, J. Jørgen Mortensen, J. Blomqvist, I. E. Castelli, R. Christensen, M. Dułak, J. Friis, M. N. Groves, B. Hammer, C. Hargus, E. D. Hermes, P. C. Jennings, P. Bjerre Jensen, J. Kermode, J. R. Kitchin, E. Leonhard Kolsbjerg, J. Kubal, K. Kaasbjerg, S. Lysgaard, J. Bergmann Maronsson, T. Maxson, T. Olsen, L. Pastewka, A. Peterson, C. Rostgaard, J. Schiøtz, O. Schütt, M. Strange, K. S. Thygesen, T. Vegge, L. Vilhelmsen, M. Walter, Z. Zeng, and K. W. Jacobsen, The atomic simulation environment—a Python library for working with atoms, Journal of Physics: Condensed Matter **29**, 273002 (2017).
[42] F. Eriksson, E. Fransson, and P. Erhart, The hiphive package for the extraction of high-order force constants by machine learning, Advanced Theory and Simulations **2**, 1800184 (2019).
[43] D. Wierstra, T. Schaul, T. Glasmachers, Y. Sun, J. Peters, and J. Schmidhuber, Natural evolution strategies, Journal of Machine Learning Research **15**, 949 (2014).
[44] H. Peng, Z.-H. Yang, J. P. Perdew, and J. Sun, Versatile van der Waals Density Functional Based on a Meta-Generalized Gradient Approximation, Physical Review X **6**, 041005 (2016), publisher: American Physical Society.
[45] G. Kresse and J. Furthmüller, Efficient iterative schemes for *ab initio* total-energy calculations using a plane-wave basis set, Physical Review B **54**, 11169 (1996).
[46] G. Kresse and J. Furthmüller, Efficiency of ab-initio total energy calculations for metals and semiconductors using a plane-wave basis set, Computational Materials Science **6**, 15 (1996).
[47] P. E. Blöchl, Projector augmented-wave method, Physical Review B **50**, 17953 (1994).
[48] G. Kresse and D. Joubert, From ultrasoft pseudopotentials to the projector augmented-wave method, Physical Review B **59**, 1758 (1999).
[49] M. Bernetti and G. Bussi, Pressure control using stochastic cell rescaling, The Journal of Chemical Physics **153**, 114107 (2020).

Supporting Information

A Morphotropic Phase Boundary in $MA_{1-x}FA_xPbI_3$: Linking Structure, Dynamics, and Electronic Properties

Tobias Hainer, Erik Fransson, Sangita Dutta, Julia Wiktor, and Paul Erhart*
Department of Physics, Chalmers University of Technology, SE-41296, Gothenburg, Sweden
* erhart@chalmers.se

Contents

Supplementary Figures **1**
S1. Training of machine-learned interatomic potential 1
S2. Evolution of weights during training 2
S3. Distribution of weights after training 2
S4. Parity plots for machine-learned interatomic potential 3

Supplementary References **3**

Supplementary Figures

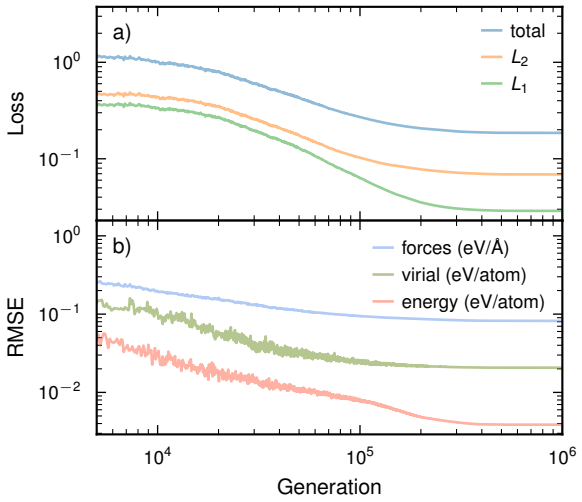

Fig. S1: Training of machine-learned interatomic potential. Evolution of (a) the total loss function $\mathcal{L}$ (blue) and the $\mathcal{L}_1$ (green) and $\mathcal{L}_2$ norms (orange) of the parameter vector as well as (b) the root mean square errors (RMSEs) of the energies $\mathcal{L}_\mathrm{e}$ (red), forces $\mathcal{L}_\mathrm{f}$ (blue), and virials $\mathcal{L}_\mathrm{v}$ (green). The total loss function is given by $\mathcal{L} = \lambda_1\mathcal{L}_1 + \lambda_2\mathcal{L}_2 + \lambda_e\mathcal{L}_\mathrm{e} + \lambda_f\mathcal{L}_\mathrm{f} + \lambda_v\mathcal{L}_\mathrm{v}$, where λ_i are hyperparameters of the optimization procedure.

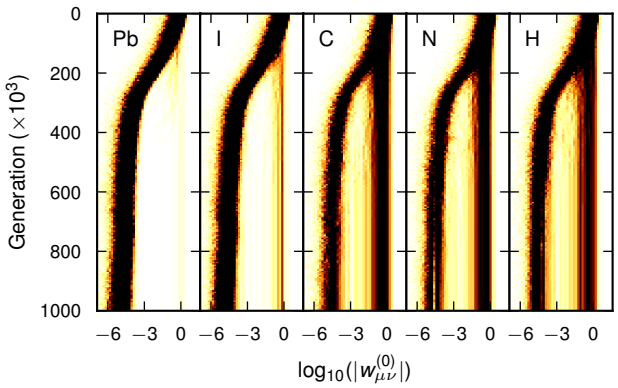

Fig. S2: Evolution of weights during training. Evolution of the absolute values of the weights $w^{(0)}_{\mu\nu}$ of the edges connecting the descriptor layer to the hidden layer of the neural network in the neuroevolution potential (NEP) model. The figure illustrates the effect of the $\mathcal{L}_1$ and $\mathcal{L}_2$ regularization terms in the NEP loss function (Figure S1), which enforce sparsity of the solution (Figure S3). By preventing accidental activation of features that were underrepresented during training during production runs this contributes to model stability and reliability.

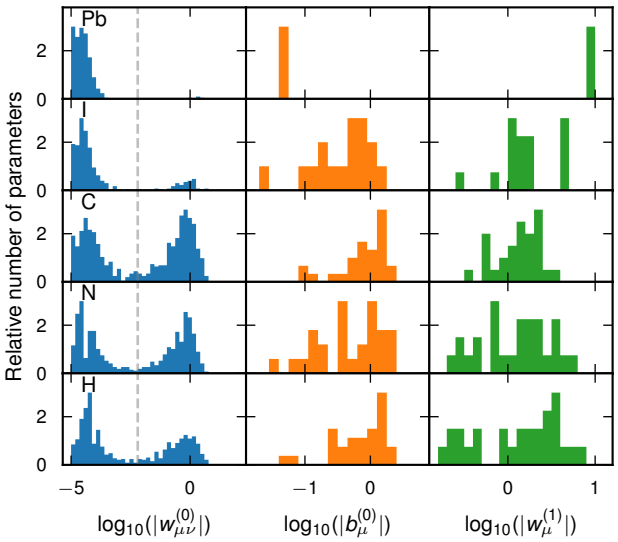

Fig. S3: Distribution of weights after training. Distribution of the absolute values of the neural network weights $w^{(0)}_{\mu\nu}$ (left), $b^{(0)}_{\mu}$ (center), and $w^{(1)}_{\mu}$ at the end of training. See Ref. 1 for the definition of these weights. The figure illustrates the effect of the $\mathcal{L}_1$ and $\mathcal{L}_2$ regularization terms in the NEP loss function (Figure S1), which enforce sparsity of the solution. The dashed vertical line in the left most column shows the separation between weights that are contributing (to the right of the vertical line) and that can be removed with negligible effect on the model scores (to the left of the vertical line). These weights can in principle be pruned and inactive edges and nodes can be pruned from the neural network, although this has not been done here.

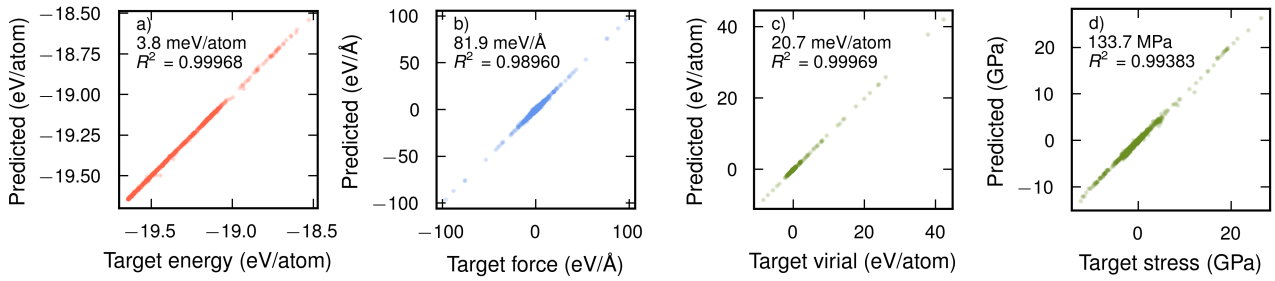

Fig. S4: Parity plots for machine-learned interatomic potential. Parity plots for (a) energy, (b) forces, (c) virials, and (d) stresses for the machine-learned interatomic potential of the NEP form constructed in this work. The insets indicate the RMSEs and coefficients of correlation (R^2).

Supplementary References

[1] Z. Fan, Y. Wang, P. Ying, K. Song, J. Wang, Y. Wang, Z. Zeng, K. Xu, E. Lindgren, J. M. Rahm, A. J. Gabourie, J. Liu, H. Dong, J. Wu, Y. Chen, Z. Zhong, J. Sun, P. Erhart, Y. Su, and T. Ala-Nissila, *GPUMD: A package for constructing accurate machine-learned potentials and performing highly efficient atomistic simulations,* The Journal of Chemical Physics **157**, 114801 (2022). doi:10.1063/5.0106617.